PROCEEDINGS, 44th Workshop on Geothermal Reservoir Engineering
Stanford University, Stanford, California, February 11-13, 2019
SGP-TR-214

Coupled Thermo-Hydro-Mechanical-Seismic Modeling of Fractured Reservoir Stimulation with Application to EGS Collab

Jianrong Lu, Ahmad Ghassemi

Reservoir Geomechanics and Seismicity Group, the University of Oklahoma, Norman, OK, 73072

ahmad.ghassemi@ou.edu

Keywords: 3D fracture network, Fracture flow, Fracture dilation and propagation, Induced seismicity, Seismic modeling

ABSTRACT

Enhanced Geothermal System (EGS) is most concerned about flow paths, induced seismicity, fracture dilation and propagation. EGS development requires an ability to accurately predict the flow paths, temperatures over time. This work first presents a framework for quantitatively predicting the behavior of fracture network, induced seismicity and flow paths in a rock mass. A fully coupled thermo-hydro-mechanical-seismic (THMS) finite element model with 3D discrete fracture network is described that is able to incorporate processes of fracture flow, rock deformation, shear dilation, fracture propagation and induced seismicity. A semi-deterministic fracture network is generated by combining the data from image logs, core with properties of fractures (e.g., length and asperity) which follow a stochastic distribution. Fracture propagation in shear/wing crack manner under injection is taken into account. This coupled method allows for multiple seismic events to occur on and around a fracture. As an application, the coupled method is applied to a COLLAB stimulation (May 24, stim-II @164 notch) to predict the flow path and induced seismicity. The model has been able to simulate the injection profile, induced seismicity and fracture propagation with good agreement with field observations.

1. INTRODUCTION

The development of EGS requires successfully stimulating a hot fractured reservoir. Fluid injected into reservoir can cause fracture network reactivation and possible propagation (Ye and Ghassemi 2018), which is often manifested as multiple MEQs. Complications from reservoir heterogeneity and complexity of flow path may lead to channeling (Rawal and Ghassemi 2014), short-circuiting, and premature thermal breakthrough so that fracture network behavior is critical to the success of EGS but there are still large uncertainties regarding direct and indirect diagnostic technologies for imaging the flow path and fracture networks. In general, geophysical surveys are the common tools for probing the subsurface structures. Numeric solutions provide a complementary method to predicate flow path, fracture network behavior and induced seismicity. In particular, numerical solutions combine with field observations and geophysical surveys to further elucidate the fundamental processes critical to EGS development.

EGS planning typically focuses on 1) accurate description of the rock mass (intact rock and 3D fracture networks), 2) detailed representation of flow in the reservoir, 3) geomechanical model to handle fracture network response to injection/production, and 4) seismic model to forecast the induced seismicity. An important challenge arising in modeling of EGS is whether to represent the fracture network explicitly (e.g., discrete fracture network) (Ucar, Berre et al. 2018, Cheng, Wang et al. 2019) or implicitly (e.g., equivalent continuum model (Pruess 1992). Numerical models with explicit representation of a fracture network have advantages over others since it can more readily handle the induced seismicity and transport phenomena. Conversely, continuum model is very desirable because it is suited for the fractured reservoir at the field scale. A hybrid method has been developed which combines the advantages from discrete fracture network and continuum models (Tezuka and Watanabe 2000, Wang and Ghassemi 2012, Cheng, Wang et al. 2019). The generation of fracture network can be classified into two categories: deterministic fracture network and stochastic fracture network. In practice, the details of individual fractures are not always available, various probabilistic framework has been utilized to characterize the stochastic distribution of fracture geometries, such as asperity and length. This means that the results in each run can be different because of the variation in fracture properties. In this work we use a semi-deterministic fracture network model that combines data derived from imaging logging and core with fracture properties which follow a stochastic distribution. An advantage of this model is that measurement data can be incorporated to constrain the uncertainties in the rock mass.

Two stimulation mechanisms may occurs concurrently during the development of EGS: 1) fracture shear slip and dilation and 2) fracture propagation. The concept of shear dilation has been called upon for EGS design, and several geomechanical models are available (Willis-Richards, Watanabe et al. 1996, Tezuka, Tamagawa et al. 2005, Wang and Ghassemi 2012, Ye and Ghassemi 2018, Cheng, Wang et al. 2019). Multiple numerical methods have been applied to model fracture networks with propagation with flow in 2D or 3D, and we use a hybrid model (Cheng, Wang et al. 2019) to take advantage of the ability to simulate fracture propagation without being restricted by the FEM mesh for the continuum portion of the problem (Cheng and Ghassemi 2017). The generation of induced seismicity is believed to evolve from rock failure in shear, and shear slip on new or pre-existing fracture planes and fracture propagation. The quasi-static model of simulating MEQ is by far the simplest and usual approach (Lee and Ghassemi 2011, Carcione, Currenti et al. 2018, Cheng, Wang et al. 2019). The effective normal and shear stress on fracture is utilized to determine the occurrence of seismic events. The magnitude of seismic events is determined by the shear modulus, fracture slip distance, and the slip area. In quasi-static models each failed fracture will generate one seismic event which is always located at the center of the fracture. In practice, a larger portion of the fracture slip is aseismic and one fracture may generate multiple seismic events located on or around the fracture (Guglielmi, Cappa et al. 2015, Amann, Gischig

et al. 2018). There is no effective way to constrain the uncertainties in the number and location of seismic events. The transition between aseismic and seismic slip is still unclear (Scotti and Cornet 1994, Senatorski 2019).

In this work, a numerical model for stimulation of a fractured reservoir is developed. It consists of four sub-models: 1) a coupled thermo-poroelastic model describing the coupling between rock deformation, fluid flow and heat flow in the fractured rock mass. 2) a semi-deterministic fracture network describing the fracture network geometry and fluid transport within the fractures. 3) a fracture dilation and propagation model to analyze fracture network deformation, and 4) a seismic model describing the events distribution and magnitude. Two threshold values are defined to illuminate the transition between the aseismic and seismic slip. The simulation outcomes include the spatial distribution of pressure changes, fracture propagation and induced seismicity. Finally, this coupled model is applied to an EGS COLLAB experiment (Kneafsey, Dobson et al. 2018) on May 24, stim-II@164 notch.

2. COUPLED THERMO-POROELASTIC MODEL

Coupled process involving poroelastic deformation, fluid flow and heat transfer occur in EGS where fractures are the primary pathways for fluid migration and production. Thus, convective heat transfer in the low permeable matrix is often insignificant (Delaney 1982) and is not considered. So that heat transfer in the reservoir is assumed to occur via fracture flow and heat conduction between rock matrix and fracture fluid. The coupled thermo-process in the rock matrix can be described in the following constitutive equations (McTigue 1986):

$$\dot{\sigma_{ij}} = 2G\dot{\varepsilon}_{ij} + \left(K - \frac{2G}{3}\right)\dot{\varepsilon}_{ij}\delta_{ij} - \alpha\dot{p}\delta_{ij} - K\alpha_m\dot{T}\delta_{ij} \tag{1}$$

$$\dot{\xi} = \alpha\dot{\varepsilon}_{kk} + \left(\frac{\alpha-\phi}{K_{sk}} + \frac{\phi}{K_f}\right)\dot{p} - \left[\alpha\alpha_m + (\alpha_f - \alpha_m)\phi\right]\dot{T} \tag{2}$$

Where $\dot{\sigma}_{ij}$ is the increment of the total stress components; $\dot{\varepsilon}_{ij}$ is the increment of the strain components; $\dot{\xi}$ is the change of fluid volume per unit reference pore volume; $\dot{p}$ and $\dot{T}$ are pore pressure change and temperature change, respectively; α is the Biot's coefficient; K is the bulk modulus; G is shear modulus; ϕ is porosity; K_{sk} and K_f are bulk modulus of rock skeleton and fluid and matrix, respectively.

The conservation equations for momentum, mass and energy are shown as:

$$\sigma_{ij,j} = 0 \tag{3}$$

$$\frac{\partial\xi}{\partial t} = \kappa p_{,jj} \tag{4}$$

$$\rho_t C_t \frac{\partial T}{\partial t} = -h_{i,i} - C_f T q_{i,i} \tag{5}$$

From the above constitutive equations and conservation equation, the coupled thermos-poroelastic field equation can be derived (McTigue 1986):

$$Gu_{i,jj} + \left(K + \frac{G}{3}\right)u_{j,ji} - \alpha p_{,j} - \gamma_1 T_{,j} = 0 \tag{6}$$

$$\alpha\frac{\partial\varepsilon_{kk}}{\partial t} + \beta\frac{\mathrm{d}p}{\mathrm{d}t} - \kappa p_{,jj} - \gamma_2\frac{\mathrm{d}T}{\mathrm{d}t} = 0 \tag{7}$$

$$\frac{\partial T}{\partial t} - c^T T_{,jj} - \left(\kappa^T T p_{,i}\right)_{,i} = 0 \tag{8}$$

A finite element method is developed for solving equation (6), (7) and (8). The details of the mathematical formulation can be found in (Zhou and Ghassemi 2009). It can be shown (Zhou and Ghassemi 2009, Lee and Ghassemi 2011, Wang and Ghassemi 2012, Cheng, Wang et al. 2019) that after spatial discretization using Galerkin method and Crank-Nicolson approximation in the time domain, the finite element matrix formula of the above equation are written as:

$$\begin{bmatrix} K_u & -C_{up} & -C_{uT} \\ C_{pu} & C_{pp} + \Delta t\theta C_{pp} & -C_{pT} \\ 0 & 0 & C_{TT} + \Delta t\theta(K_{cdT} + K_{cvT}) \end{bmatrix}\begin{bmatrix}\Delta u \\ \Delta p \\ \Delta T\end{bmatrix} = \begin{bmatrix} \Delta t\dot{F}_u \\ \Delta tF_{qin} - \Delta tK_p p_{t-\Delta t} \\ \Delta tF_{hin} - \Delta t(K_{cdT} + K_{cvT})T_{t-\Delta t}\end{bmatrix} \tag{9}$$

Where $\Delta u, \Delta p$ and ΔT are the vectors of unknowns variables; $\Delta t = t_n - t_{n-1}$ is the time step size; θ is a scalar parameter and set to be 1.0 in this work; F_u, Fq and F_h are the external load, fluid and heat source terms; $p_{t-\Delta t}$ and $T_{t-\Delta t}$ is the pore pressure and temperature of the previous time step. Other matrix are described in (Cheng, Wang et al. 2019). By solving the Equation 9 with initial and boundary conditions, the primary unknowns of displacement u , pore pressure p and temperature T can be resolved directly.

3. FRACTURE NETWORK MODEL

3.1 Fracture Network Generation

In this work, a semi-deterministic fracture network is generated by combining the data from imaging logging, core and stochastic fracture properties (e.g., length and asperity). Fracture networks are extremely variable and almost difficult to detect in the subsurface. As a result,

stochastic model are used to describe the fracture network geometry (Willis-Richards, Watanabe et al. 1996, Rahman, Hossain et al. 2002, Wang and Ghassemi 2012, Lu and Ghassemi 2017, Cheng, Wang et al. 2019). Fracture lengths are regarded to follow Log Normal distribution in this work (Long, Remer et al. 1982, Dershowitz and Einstein 1988). The fractures can be treated as penny shape or elliptical. Fracture apertures follow a power law distribution (Laubach, Hooker et al. 2014). The fracture network realizations are thus inherently non-unique and inevitably impact the results in each run. Geophysical surveys, as well as core and outcrop, still provide some valuable information to constrain the uncertainties in the generation of fracture network (Knox, Ajo-Franklin et al. 2016, den Boer and Sayers 2018). For instance, fracture orientation could be extracted from the borehole image logging and core (see Figure 1).

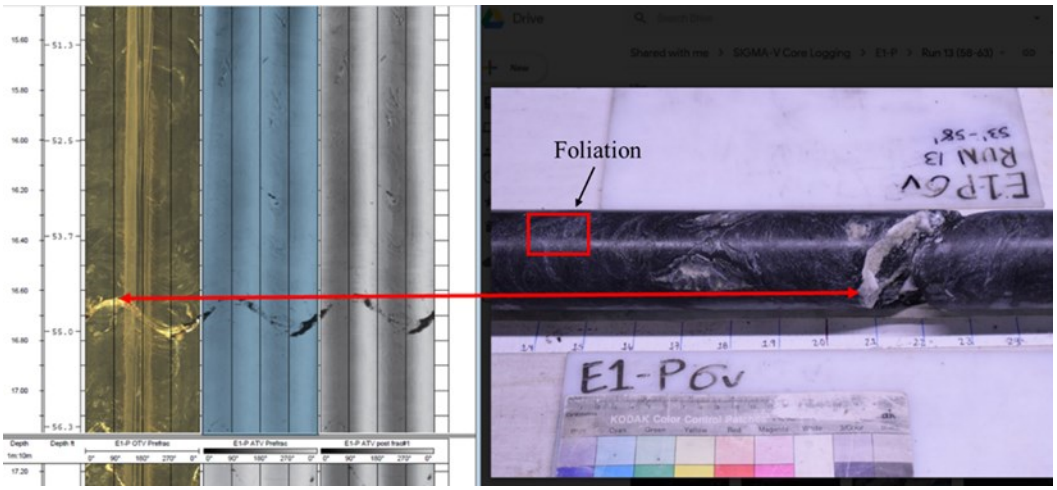

Figure 1: Acoustic televiewer log showing the trace of the facture zone in borehole E1-P from Collab EGS.

Although borehole imaging logging and core only map a small zone around the wellbore, they are still utilized as a reference for fracture orientation. In the intermediate-scale experiments, the number and location of detected fractures from borehole imaging logging and core (Kneafsey, Dobson et al. 2018, Ulrich, Dobson et al. 2018) are considered the same as the real system. However, they are still foliations (See Figure 1) which also affect the rock mass response to water injection. In this work, a dual-scale fracture network is implemented. A large scale fracture network, referred to as the large-scale facture population (derived from the borehole image logs and core) and a small-scale fracture network referring to the micro-crack population. Micro-cracks are assumed to accompany each major fracture and are located around them (See Figure 2a). The major fracture population is explicitly represented. Thus, major fracture deformation and pressure can be accurately obtained. While the distribution of micro-cracks is implicitly represented and depends on the major fracture roughness and a distance function reflecting distance from the major fracture. We attempt to mesh ellipsoids around major fractures to place micro-cracks within them. The nodes of the mesh are considered as the location of micro-cracks. The major fractures are engulfed by the ellipsoid whose major and minor axes are perpendicular to the fractures. In this work, we assume that the ellipsoid half height, half length, and half width equal to 1.5, 1.5, and 0.5 times the major fracture radius, respectively. The distance function associated with a point p_j and the fracture F_i is given by:

$$d_i(p_j) = \text{Shortestdistance}(F_i, p_j) \tag{10}$$

Where p_j represents the vertices of the ellipsoid and the major fracture. The size of element of ellipsoid mesh is given by:

$$h(p_j) = \min(l_{min} + s \cdot d_i(p_j), l_{max}) \tag{11}$$

where $h(p_j)$ is the element size at point p_j ; l_{min} and l_{max} are the minimum and maximum allowable element size respectively. s is the scaling of the element size, $h(p)$ is submitted to GMSH (Geuzaine and Remacle 2009) to mesh the ellipsoid. Thus, the closer the location to the major fracture, the higher the density of micro-crack population at that location (see Figure 2a). Here we also argue that the major fracture roughness affects the distribution of micro-cracks. For example, major fracture F_1 can be divided into four patches and each patch is assigned a joint roughness coefficient (JRC) (Barton and Choubey 1977) (see Figure 2b). In the same situation, peak shear strength is increased with increasing the JRC (Barton and Choubey 1977). The sliding of the high shear strength fractures may active more micro-cracks off the fracture plane. Thus we assumed that JRC of any patch is lesser than 5, the density of micro-cracks is considered as zero (see Figure 2b).

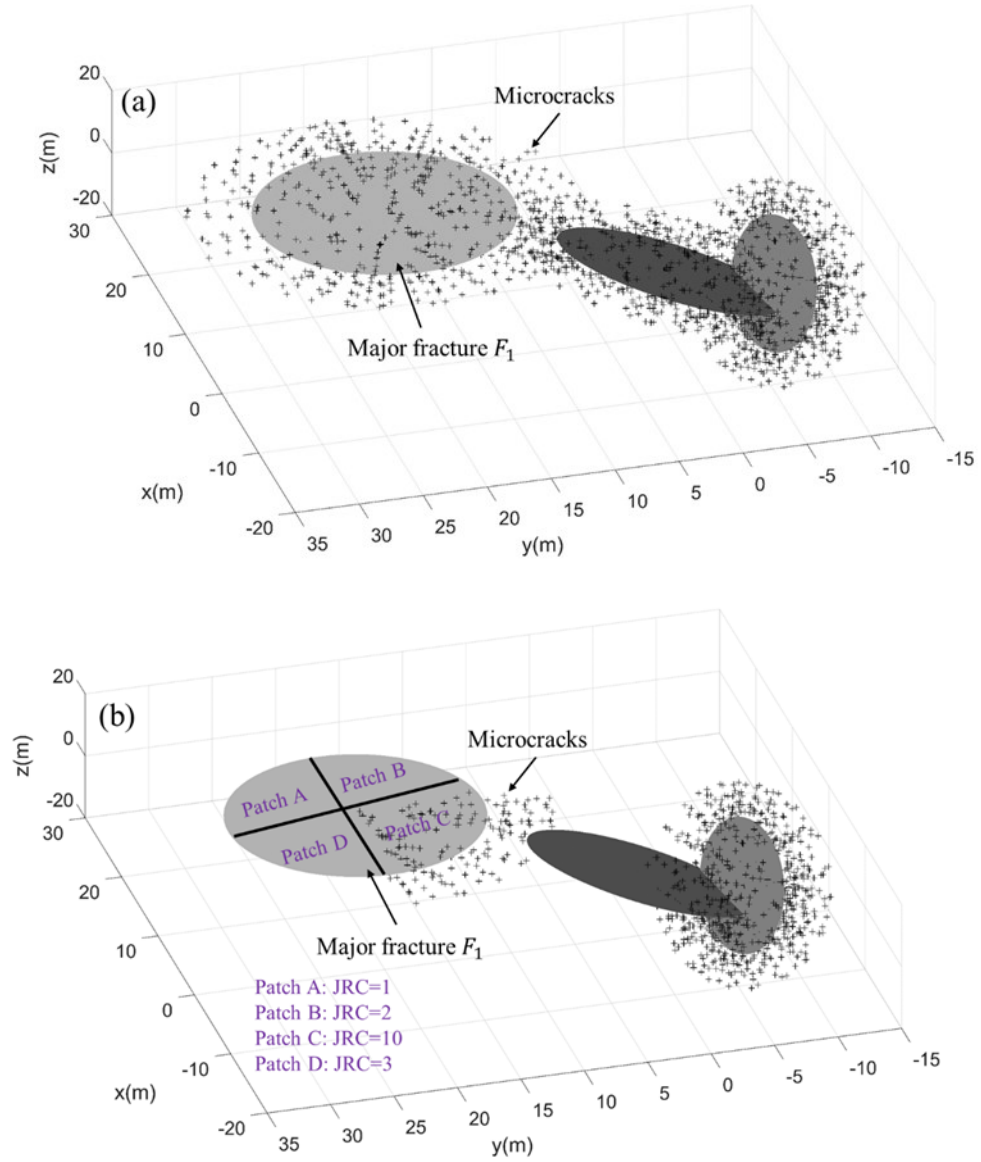

Figure 2: a) original distribution of major fractures and micro-cracks. b) A distance function and fracture surface heterogeneity is imposed on the distribution of major factures and micro-cracks.

3.2 Flow in Fractures

After a 3D semi-deterministic fracture network is generated, a fracture flow model is defined. The fracture permeability is defined using the cubic law and the overall rock mass permeability is calculated as the equivalent permeability concept. Here the permeability of the micro-cracks are included in that of the matrix. The intersection line between the fractures and finite elements faces are calculated based on a geometric surface-surface intersection algorithm (Wang 2014, Cheng, Wang et al. 2019). The permeability tensor on a finite element can be calculate as

$$k_i = \sum_{j=1}^{n_{fi}} \frac{a_j^3 l_{ij}}{12 A_i}, i = x, y, z \tag{12}$$

Where n_{fi} is the total number of fractures in the element; a_j is the aperture of the j^{th} fracture; l_{ij} is the length of intersection line on the element interface; A_i is the cross-section area in the corresponding i direction.

During injection, the pressure and temperature inside the fracture network change, which alters the stress distribution around fractures and affects the deformation behavior of fractures. Each connected fracture is treated as a 1D flow pipe connecting the fracture center and

the mid-point of the intersection with an adjacent fracture. By applying the Mohr Coulomb failure criterion to the Patton's saw tooth fracture model, the total stimulated fracture aperture (Willis-Richards, Watanabe et al. 1996) is written as:

$$a = \frac{a_0}{1+9\sigma_{eff}/\sigma_{nref}} + a_s + a_{res} \tag{13}$$

Where a_0 is the initial effective aperture; a_s is the aperture change due to shear slippage; and a_{res} is the residual aperture at high effective stress. The residual aperture a_{res} is assumed to be zero in this work. The detail of calculation of pressure, temperature distribution within fracture network, fracture shear slippage can be checked in (Cheng, Wang et al. 2019). It is postulated in this work that a fracture will either propagate in its own plane, or it will propagate by wing cracks.

3.3 Induced Seismicity

Slip on fractures is believed to induce seismic events. In in-situ experiment on the intermediate scale (e.g., decameter scale) (Guglielmi, Cappa et al. 2015), show that injection induce fracture slip can enhance the permeability by up to 2-3 orders of magnitude and larger portion of slip is aseismic. Aseismic-seismic transition exhibits a dependence on the slip rate and dilation (Amann, Gischig et al. 2018, Ye and Ghassemi 2018). When either the fracture slip distance, or the fracture slip rate, or both are larger than threshold values in a cycle (or critical stiffness $k_c = (\mu_s - \mu_d) \cdot \sigma_n / D_c$ is less than shear stiffness k(Scholz 2002)), the fracture will become unstable (seismic). Some previous works (Barton, Bandis et al. 1985) indicated that if the shear slip is larger than the peak displacement δ_p, the fracture becomes unstable:

$$\delta_p = \frac{L}{500}\left(\frac{JRC}{L}\right)^{0.33} \tag{14}$$

So, we use the more convenient modeling approach, i.e., if the slip rate is larger than a certain value, we assume the shear stiffness is less than the critical stiffness k_c. So, the threshold slip displacement and slip rate are utilized to distinguish between the aseismic and seismic slip (Meng and Wang 2018).

It is generally accepted that induced seismicity is governed by the Mohr-Coulomb failure criteria and one event occurs upon the failure the fracture. In practice, one fracture may generate multiple events on or surrounding the fracture. Numerical generation of induced seismicity has been intensely studied, yet few models exist capable of achieving induced seismic events with realistic quantitative output. Those simulations cannot resolve the number and location and magnitude of multiple seismic events due to a fracture failure. It is known that most closed seismic events in the fields are made up of many smaller-scale ruptures of one major fracture and surrounding micro-cracks (Hu and Ghassemi 2018, Ye and Ghassemi 2019). Those multiple events occur close to each other in space and time. In this work, we propose a new model of seismic generation. Once a major fracture fails based on the Mohr-Coulomb failure criterion, there is one event generated at the fracture (center). This event can be referred to original numerical event. The magnitude of original numerical event is calculated as (Hanks and Kanamori 1979, McGarr, Spottiswoode et al. 1979):

$$M_0 = \int_{\Sigma} G U_s \mathrm{d}A \tag{15}$$

Where M_0 is the seismic moment; G is the shear modulus and U_s is shear displacement (seismic). A is the slip area and here is treated as the area of fracture. The magnitude of original event M_w generated by shear slippage can be estimated as:

$$M_w = \frac{2}{3}\log_{10} M_0 - 10.7 \tag{16}$$

The seismic energy of an event can be calculated as:

$$\log_{10} E_R = 4.8 + 1.5 \cdot M_w \tag{17}$$

The seismic energy E_R is the lumping of all seismic energy from this fracture. Next, we calculate the shear stress and normal stress on the micro-cracks (the orientation of micro cracks may follow a randomly distribution or a certain stochastic distribution e.g., Log normal distribution). The density of micro cracks is defined following Section 3.1. The micro-cracks friction angle is treated the same as the major fracture and micro-cracks cohesion is set to zero in this paper. There is one potential seismic event on the failed micro-cracks based on the Mohr Coulomb failure criterion. Thus, there may be an event cloud surrounding a major fracture. It is known that Gutenberg-Richter law expresses the relationship between the magnitude and total number of events in any given region. Thus, each event should follow the Gutenberg-Richter law suggesting that those events cloud have the same as b-values. Here a-value is used as a fitting constant. The Gutenberg-Richter law on the ith failure fracture can be represented as:

$$\log_{10} N = a_i - b \cdot M \tag{18}$$

Where N is the number of events having a magnitude larger or equal to the magnitude M. b value can be obtained from the field observation. a_i is the fitting number and calculated as:

$$a_i = b \cdot M \tag{19}$$

Where M is the magnitude of original numerical event and obtained from equation 16. The magnitude of nth event is calculated as:

$$M_n = \frac{a_i - \log_{10} n}{b} \tag{20}$$

Where M_n is the magnitude of nth event and a_i is from equation 19. The seismic energy of nth event is calculated as:

$$(E_R)_n = \exp(4.8 + 1.5 \cdot M_n) \tag{21}$$

Equation 18 can theoretically be used to generate an infinite number of events and some constrains are needed to limit the number of events. The first prescribed condition is the energy conservation i.e., the total seismic energy of the event cloud should be less than the seismic energy of the original numerical event:

$$\sum_{j=1}^{n} (E_R)_j \leq (E_R)_{origin} \tag{22}$$

Where $\sum_{j}^{n} (E_R)_j$ is the total seismic energy of the event cloud; $(E_R)_{origin}$ is the seismic energy of the original event. Another condition is that the geophones cannot detected very small-magnitude events. So, there is a threshold magnitude imposed. Such a threshold magnitude of event M_{th} is set as -3 in this work:

$$M_n \geq M_{th} = -3 \tag{23}$$

These two conditions can constrain the number of generated events in the model. The stress and pore pressure fields of micro-cracks can be obtained by interpolating the stress and pressure distribution on the finite elements. Micro-cracks failure is assessed based on the Mohr-Coulomb failure criterion. In generally, the number of failing micro-cracks is larger than the number of events. Each failing micro-crack can have one event. The events are assumed to locate on the micro-cracks which are closest to the major fracture. Because the effective maximum stress of micro-cracks are greatly decreased in the vicinity of the major fracture due to the high pore pressure in the vicinity of the major fracture. The event is closer to accompany major fracture, the magnitude of event is larger. Other critical micro-cracks are far from the major fracture and seismic energy of those micro-cracks are very small and those micro-cracks are considered as aseismic.

3.4 Integration with the Coupled FEM

The fracture network model is integrated with the coupled thermo-poroelastic FEM by linking the permeability change with fracture deformation. At each time step, fracture aperture and length data are input in FEM for equivalent permeability calculations. The stress and pore pressure required for fracture deformation analysis (e.g., slippage and propagation) are calculated from the FEM solutions. Once fractures deformations, there apertures and length are updated, the solution proceeds to the next time step. The step-by-step solution procedure for the integrated model is shown in Figure 3.

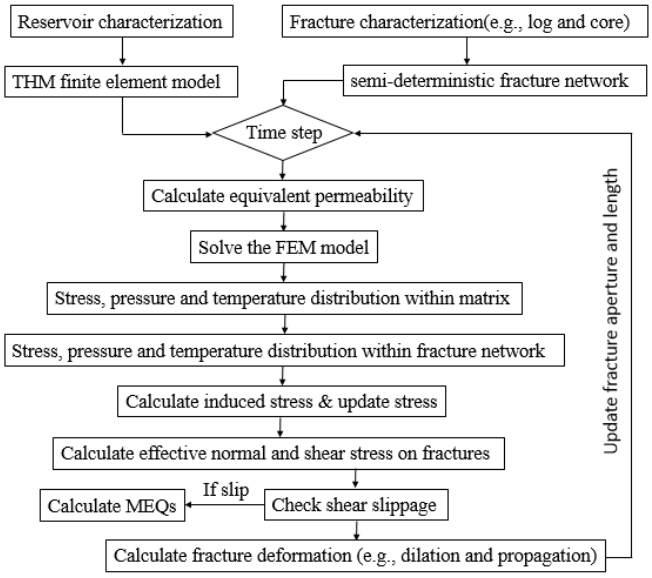

Figure 3: flowchart of the integrated model.

4. EGS COLLOB PROJECT

An objective of this project is to understand and predict permeability enhancement and evolution in crystalline rock in response to hydraulic fracturing, and how to create sustained and distributed permeability for heat extraction. The Stanford Underground Research Facility (SURF) in Lead, South Dakota is the EGS Collab project experimental site (Figure 4). The designated testing depth is ~4850 feet with a temperature of (~30-35° C). A series of measurements (e.g., sewer camera, acoustic televiewer log and pressure gauge) have been conducted in the boreholes (Roggenthen and Doe 2018, Ulrich, Dobson et al. 2018). Stress measurements as part of kISMET have indicated the S_{hmin} is about 21.7MPa and is oriented N4W, and the S_{Hmax} is about 35.5MPa and is oriented N86E. The vertical stress is

considered to be lithostatic and equal to 41.8 MPa. The initial pore pressure is set to zero in this work. Figure 5 shows the injection, production and monitoring wells; E1-I and E1-P are the injection well and the production well, respectively. The geophysical monitoring instrumentation occupies the remaining six boreholes. Radial notches in the injection borehole, provide initiation points for tensile hydraulic fractures that will propagate to the production well E1-P and support tracer tests and heat-exchange circulation experiments.

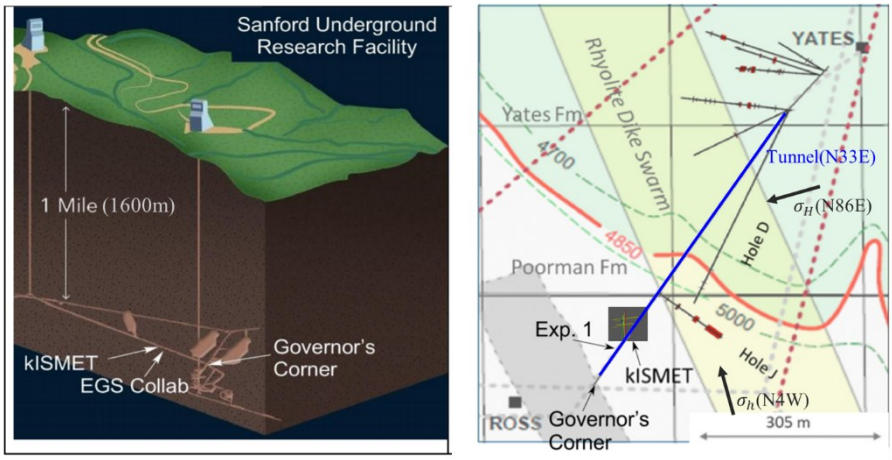

Figure 4: A) schematic view of the Stanford Underground Research Facility (SURF) and EGS Collab. B) Geologic map of the 4850 feet of SURF in the vicinity of the EGS Collab. The minimum horizontal stress σ_h is oriented N4W and maximum horizontal stress σ_H is oriented N86E.

In this work, we simulate the Stim-II HF@164 notch at E1-I which occurred on May 24. The injection began on May 24, 22:00 and ended on May 24, 22:53. The detailed injection profile is illustrated in Figure 5. The simulation domain used to represent the Collab EGS is 100 m in the E-W direction (x-axis), 100 m in the N-S direction (y-axis), and 100 m in the vertical direction (z-axis). The center of the simulation domain is defined as the average of all fracture centers coordinates ([815.7, -1307.2, 109.8] m in homestake coordinates). Image logs and core data have shown 112 major fractures in Collab EGS and most of fractures have large dip (Ulrich, Dobson et al. 2018) (Figure 6a). The distribution of micro-cracks is not shown in Figure 6a. During the injection, 203 events were detected (Figure 6b). The mechanical properties were taken from others works (Oldenburg, DOBSON et al. 2016, Morris, Fu et al. 2018) (Table 1):

Table 1. Reservoir properties used in model.

Parameter value	**Values**	**Source/Comments**
Young's Modulus	$71GPa$	Oldenburg et al. 2016
Drained Poisson's Ratio	0.22	Oldenburg et al. 2016
Undrained Drained Poisson's Ratio	0.46	Assumed
Biot's Coefficient	1.0	Assumed
Vertical stress S_V	$41.8MPa$	Oldenburg et al. 2016
Maximum horizontal stress $S_{\mathrm{h}max}$	$35.5MPa$	Oldenburg et al. 2016
Minimum Horizontal stress $S_{\mathrm{h}min}$	$21.7MPa$	Oldenburg et al. 2016
Initial pore pressure	$0.0MPa$	Assumed
Matrix Permeability	$0.05mD$	Assumed
Dilation angle	$0.035rad$	Assumed
Fracture radius (lognormal distribution)	$mean = 5(m)\ \ variance = 1$	Assumed

Fracture asperity(lognormal distribution)	$mean = 6 \cdot 10^{-5}(m)\ \ variance = 10^{-6}$	Assumed
Cohesive(lognormal distribution)	$mean = 3MPa\ variance = 10^{6}$	Assumed
Frictional angle(lognormal distribution)	$mean = 0.5(rad)\ variance = 0.01$	Assumed
Mode I fracture toughness	$1MPa\sqrt{m}$	Morris et al. 2016

In this work, we follow the injection rate from May 24, 22:00 to May 24, 22:53. Cold water is injected from the notch@164 in E1-I using injection rate control. It is assumed that the temperature of injection water is the same as the reservoir. Therefore, the cooling effect is neglected. Figure 5 shows the comparison between the simulation pressure/injection rate and the pressure/injection rate measured at the field. The discrepancy is caused by the fact that pressure-aperture coupling is not fully considered in the current network model.

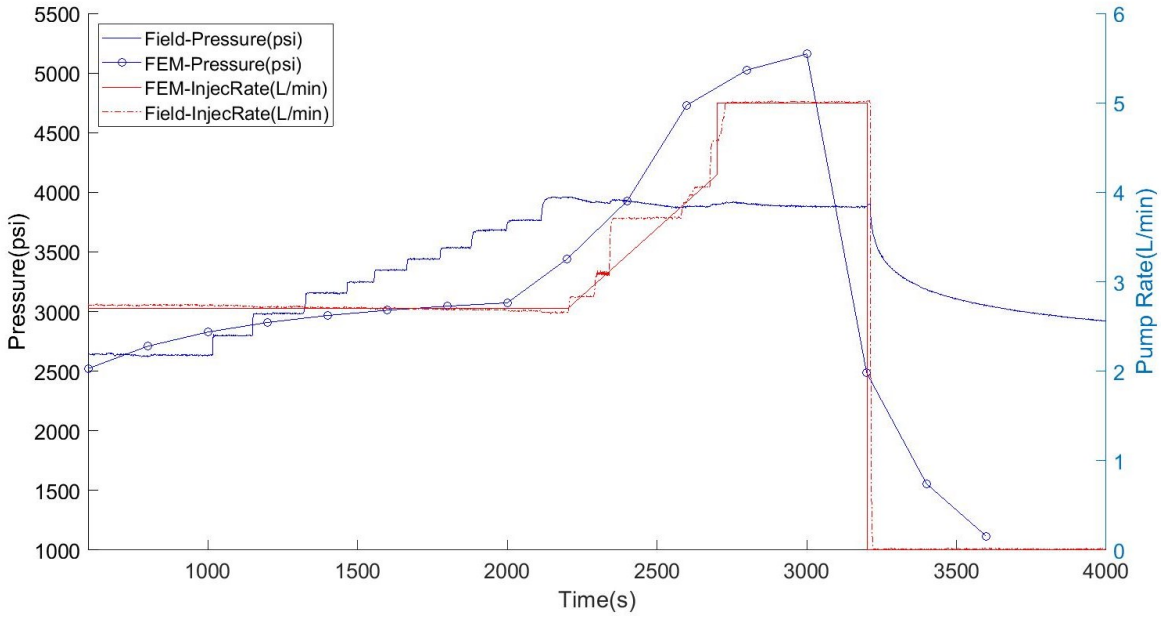

Figure 5: pressure and injection rate at 164@notch. The resulting pressure trend generally agrees with field measured values.

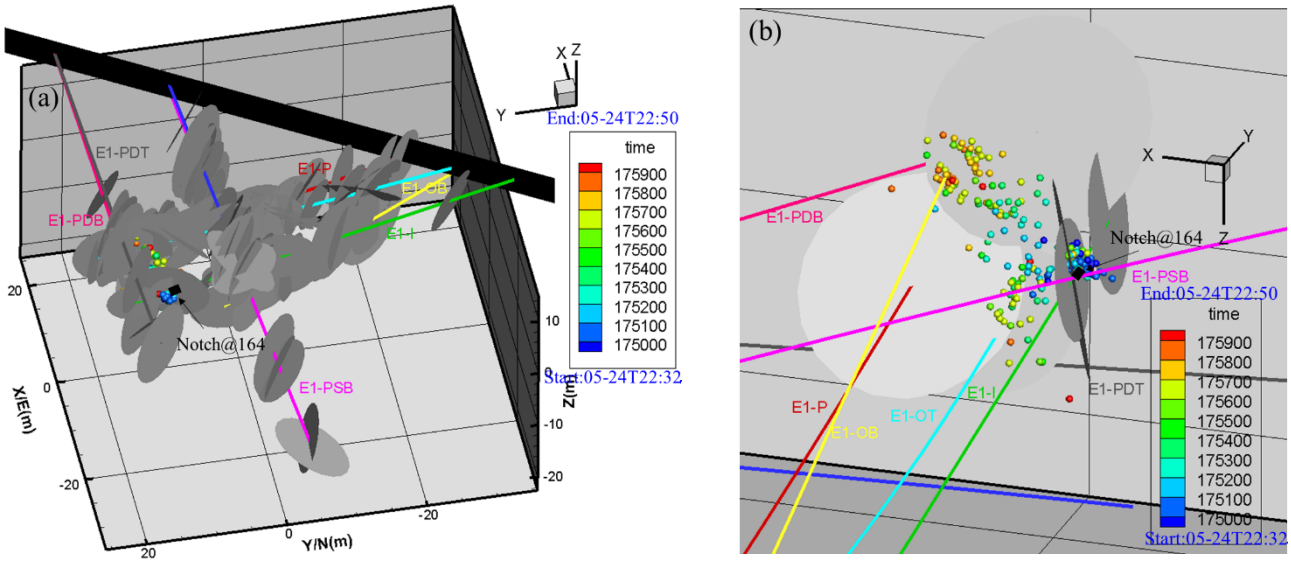

Figure 6: a semi-deterministic fracture network and field-observed MEQs occurs from May 24, 22:32 to May 24, 22:50. The number of fracture is 112 and the number of field-observed MEQs is 203.

The calculated pore pressure distribution within the reservoir and the fracture network at 22:40 is shown in Figure 7. The location of the water source is located at Notch@164 at E1-I. The center of I-164 and the notch share the same location. Thus I-164 is considered as the primary conduit because of the low permeability of the rock matrix. Fracture I-164, I-183 and PDB-130 intersect each other, and the lengths of the intersections are relatively long. Thus the permeability of the network consisting of I-164, I-183 and PDB-130 is large according to the Equation 12. The initial aperture of the major fractures, such as I-164, I-183 and PDB-130 are approximately the same (See Table 1). Furthermore, simulations show the fracture I-164 and PDB-130 experience dilation during injection. Figure 7 suggest that PDB-130 is slightly connected with OT-143 and the length of intersected segment is relatively short. The aperture of the fracture OT-143 remains the same during the injection according to simulations. Thus little water flows from PDB-130 to OT-143. The pressure in fractures observed in the hole E1-OT are relatively low. The Fracture network data show OT-143 is also connected with P-128, P-122 and some other fractures. Thus, it seems very little fluid can flow into the P-122. So, Figure 7 suggests that pore pressure development is mostly controlled by the fracture network connectivity. The flow path between the injection and production well can be defined as: Notch@164 to I-183/PDB-130 to OT-143 to P-128/122 as shown by the arrows.

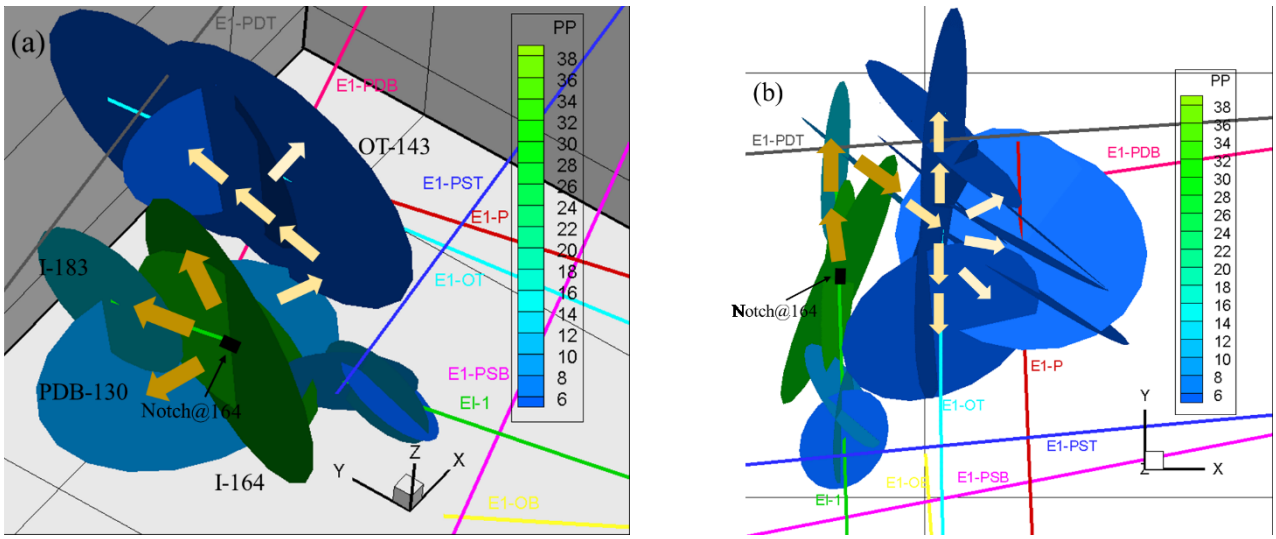

Figure 7: flow path is created by injection. The source is located at notch@164. Since fracture I-164, PDB-130 and I-183 is connected to each other, those fractures are the major components of circulation. Fracture PDB-130 is slightly connected to OT-143 and only small volume of fluid flows to OT-143. The flow rate of fractures on E1-OT and E1-P may be low.

Numerical simulations show during injection, only fracture I-164, PDB-130, OT-153 and P-128 experienced dilation and increased aperture. The initial stimulated fracture aperture of I-164, PDB-130, OT-153 and P-128 is $6.3\cdot 10^{-6}$, $6.6\cdot 10^{-6}$, $5.3\cdot 10^{6}$ and $4.4\cdot 10^{-6}$m,

respectively. The stimulated fracture aperture of I-164, PDB-130, OT-153 and P-128 at 22:40 is $1.3\cdot 10^{-5}$, $7.2\cdot 10^{-6}$, $5.7\cdot 10^{-6}$ and $5.3\cdot 10^{-6}$m, respectively. As a result, the permeability of those four fractures increases because it is critically dependent on the third power of apertures (see Equation 13). Only a few fractures show permeability improvement because of the short period of injection. The fracture I-164 has propagated in its own plane and increased its radius from 5 m to 6.8m (Figure 8). No wing crack is generated in this simulation. The propagation of I-164 may not stimulate the reservoir because I-164 does not create new connection with other fractures.

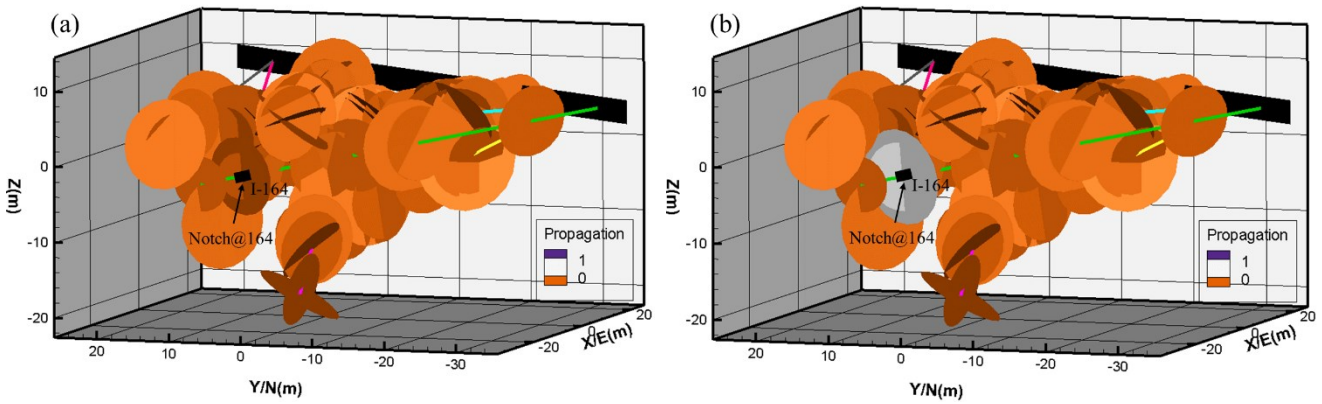

Figure 8: fracture propagation under injection. Fracture I-164 are originally 3.20 and 5.30 m radius, respectively. At final time step, fracture I-164 are 4.69 and 6.44 m radius, respectively.

In this simulation, four facture slipped. The number of generated MEQ events was obtained by following the methodology of Section 3.3. Figure 9a~c show a comparison between the simulated MEQs and field-observed MEQs. The number of the simulated MEQs and field-observed MEQs are 231 and 202, respectively. Most field-observed MEQs are distributed in the zone between PDB-130 and I-164 (see Figure 9b). Simulated MEQs match only some of the field-observed MEQs in this zone because the semi-deterministic fracture network may not reflect the actual rock mass condition. Some foliations and small fractures may be present in this zone that could have been stressed and/or pressurized during injection. Figure 9a~c still indicates that the distribution of simulated MEQs has a good agreement with the field-observed MEQs. In Figure 9d, we use the Gutenberg-Richter law (a=0.5 and b=0.62) to fit the simulated MEQs very well. b-value is kept constant while a-value is fitting number. Previous works attempted to apply the location of MEQs to estimate permeability and fracture orientation (Shapiro, Huenges et al. 1997, Lu and Ghassemi 2019). The Gutenberg-Richter law (GR law) expresses the correlation between the magnitude and the total number of events. The information of GR law could be extracted from the field data to further characterize the stimulated reservoir.

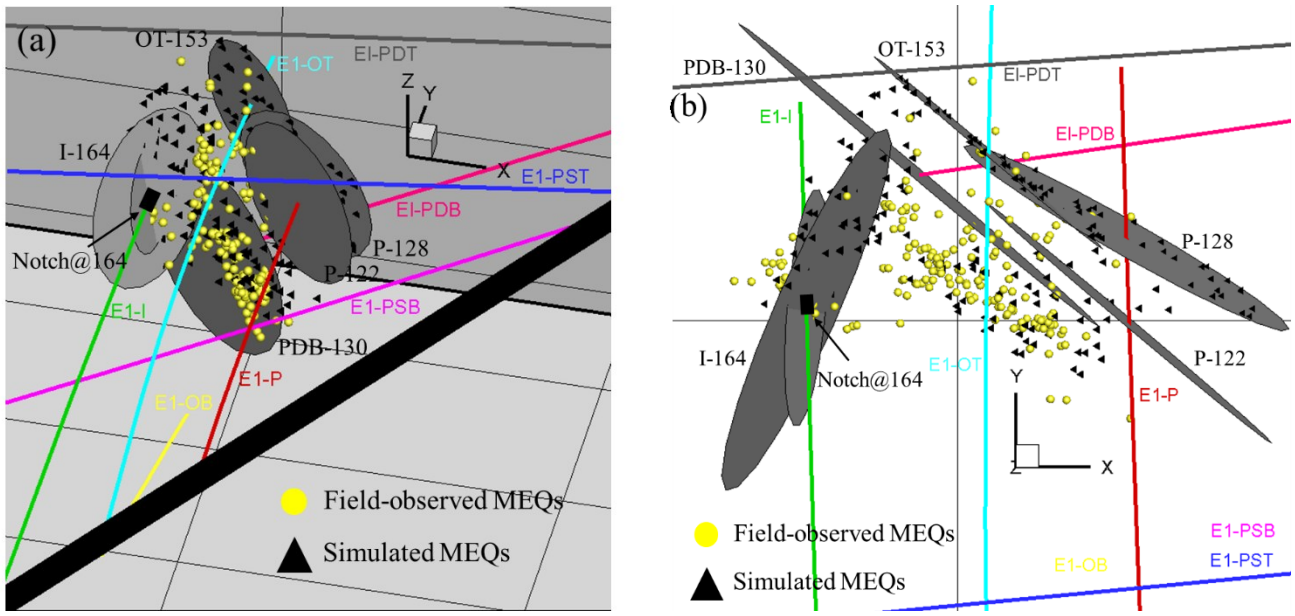

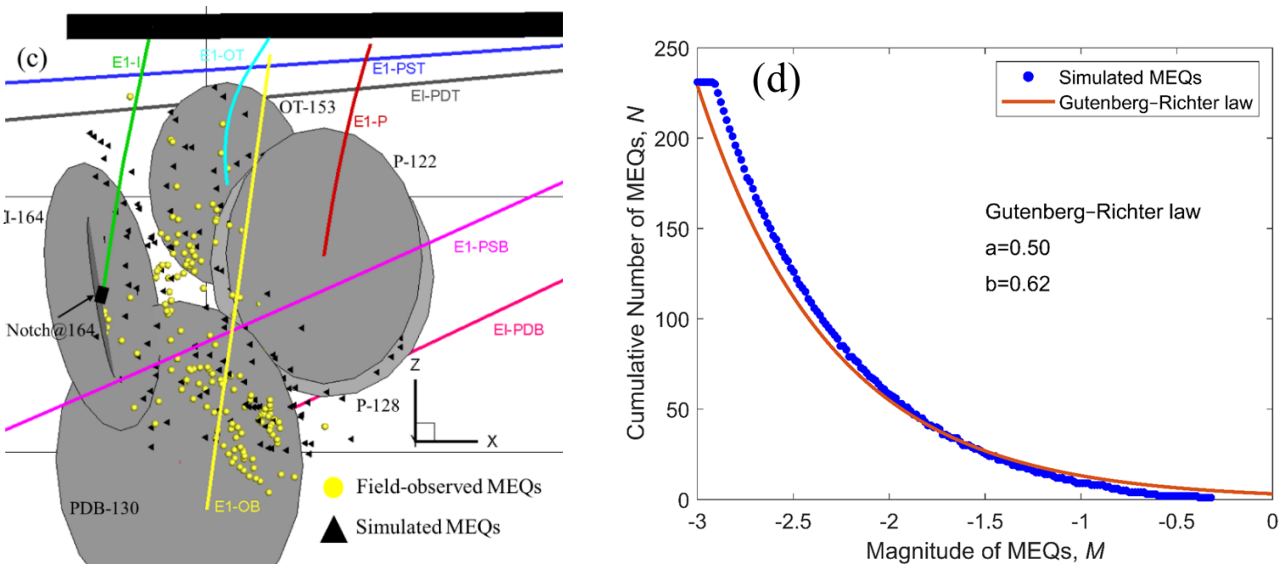

Figure 9: Comparison between simulated MEQs with field-observed MEQs. (a)~(c) the distribution of simulated MEQs and field-observed MEQs. (d) The magnitude-frequency distributions and seismic b-values for simulated MEQs. Because a-value is a fitting number, and the b-value is influenced by the numerical model, there are differences between field-observed MEQs and simulated MEQs.

5. CONCLUSION

In this work, a conceptual numerical model has been developed to simulate the response of COLLAB Testbed 1 to water injection. The coupling process between behavior of fracture network, fracture flow, fracture dilation and propagation, and induced seismicity is described using a fully coupled THMS FEM model. A semi-determinist fracture network generated by combining data derived from imaging logging and core with fracture properties which follow a stochastic distribution. An advantage of this semi-determinist fracture network model is that measurement data can be incorporated to constrain the uncertainties in the rock mass. Another advantage of this network model is that micro-cracks are also considered. Integration between the coupled finite element model and the semi-determinist fracture network model is achieved by linking permeability change with fracture deformation (e.g., dilation and propagation). A stress dependent fracture deformation model with a shear dilation model is utilized to account for shear dilation. An analytic approach for fracture propagation is applied using the maximum tensile stress criterion. The induced seismicity during injection process are also evaluated. A seismic model is developed which allow for multiple seismic events to occur on and around a fracture. Two conditions are imposed to constrain the number of events. The switching conditions between aseismic slip and seismic slip are also resolved. The simulation results (e.g., injection profiles and induced seismicity) of the Stim-II 164@notch on May 24 show trends similar to the field observations.

6. ACKNOWLEDGMENTS

This material was based upon work supported by the U.S. Department of Energy, Office of Energy Efficiency and Renewable Energy (EERE), Office of Technology Development, Geothermal Technologies Office and the OU Reservoir Geomechanics JIP. The research supporting this work took place in whole or in part at the Sanford Underground Research Facility in Lead, South Dakota. The assistance of the Sanford Underground Research Facility and its personnel in providing physical access and general logistical and technical support is acknowledged.

REFERENCES

Amann, F., V. Gischig, K. Evans, J. Doetsch, R. Jalali, B. Valley, H. Krietsch, N. Dutler, L. Villiger, B. Brixel, M. Klepikova, A. Kittilä, C. Madonna, S. Wiemer, M. O. Saar, S. Loew, T. Driesner, H. Maurer and D. Giardini (2018). "The seismo-hydromechanical behavior during deep geothermal reservoir stimulations: open questions tackled in a decameter-scale in situ stimulation experiment." Solid Earth **9**(1): 115-137.

Atapour, H. and M. Moosavi (2014). "The Influence of Shearing Velocity on Shear Behavior of Artificial Joints." Rock Mechanics and Rock Engineering **47**(5): 1745-1761.

Barton, N., S. Bandis and K. Bakhtar (1985). "Strength, deformation and conductivity coupling of rock joints." International Journal of Rock Mechanics and Mining Sciences & Geomechanics Abstracts **22**(3): 121-140.

Barton, N. and V. Choubey (1977). "The shear strength of rock joints in theory and practice." Rock mechanics **10**(1): 1-54.

Carcione, J. M., G. Currenti, L. Johann and S. Shapiro (2018). "Modeling fluid injection induced microseismicity in shales." Journal of Geophysics and Engineering **15**(1): 234-248.

Cheng, Q. and A. Ghassemi (2017). Numerical Modeling of Fluid Flow, Heat Transfer and Induced Mircoseismicity in Three Dimensional Fracture Networks. 51st U.S. Rock Mechanics/Geomechanics Symposium. San Francisco, California, USA, American Rock Mechanics Association**:** 9.
Cheng, Q., X. Wang and A. Ghassemi (2019). "Numerical simulation of reservoir stimulation with reference to the Newberry EGS." Geothermics **77**: 327-343.
Cotterell, B. and J. R. Rice (1980). "Slightly curved or kinked cracks." International Journal of Fracture **16**(2): 155-169.
Delaney, P. T. (1982). "Rapid intrusion of magma into wet rock: Groundwater flow due to pore pressure increases." Journal of Geophysical Research: Solid Earth **87**(B9): 7739-7756.
den Boer, L. D. and C. M. Sayers (2018). "Constructing a discrete fracture network constrained by seismic inversion data." Geophysical Prospecting **66**(1): 124-140.
Dershowitz, W. S. and H. H. Einstein (1988). "Characterizing rock joint geometry with joint system models." Rock Mechanics and Rock Engineering **21**(1): 21-51.
Geuzaine, C. and J.-F. Remacle (2009). "Gmsh: A 3-D finite element mesh generator with built-in pre- and post-processing facilities." International Journal for Numerical Methods in Engineering **79**(11): 1309-1331.
Guglielmi, Y., F. Cappa, J.-P. Avouac, P. Henry and D. Elsworth (2015). "Seismicity triggered by fluid injection–induced aseismic slip." Science **348**(6240): 1224.
Gutierrez, M. and D.-J. Youn (2015). "Effects of fracture distribution and length scale on the equivalent continuum elastic compliance of fractured rock masses." Journal of Rock Mechanics and Geotechnical Engineering **7**(6): 626-637.
Hanks, T. C. and H. Kanamori (1979). "A moment magnitude scale." Journal of Geophysical Research: Solid Earth **84**(B5): 2348-2350.
Hu, L. and A. Ghassemi (2018). Heat and Fluid Flow Characterization of Hydraulically Induced Fracture in Lab-Scale. 52nd U.S. Rock Mechanics/Geomechanics Symposium. Seattle, Washington, American Rock Mechanics Association**:** 7.
Jung, R. (2013). EGS—goodbye or back to the future. ISRM International Conference for Effective and Sustainable Hydraulic Fracturing, International Society for Rock Mechanics and Rock Engineering.
Kneafsey, T. J., P. Dobson, D. Blankenship, J. Morris, H. Knox, P. Schwering and M. White (2018). An Overview of the EGS Collab Project: Field Validation of Coupled Process Modeling of Fracturing and Fluid Flow at the Sanford Underground Research Facility, Lead, SD. PROCEEDINGS, 44th Workshop on Geothermal Reservoir Engineering, Stanford University, Stanford, California.
Kneafsey, T. J., P. F. Dobson, J. B. Ajo-Franklin, C. Valladao, D. A. Blankenship, H. A. Knox, P. Schwering, J. P. Morris, M. Smith, M. D. White, T. Johnson, R. Podgorney, E. Mattson, G. Neupane, W. Roggenthen and T. Doe (2018). The EGS Collab Project: Stimulation and Simulation. 52nd U.S. Rock Mechanics/Geomechanics Symposium. Seattle, Washington, American Rock Mechanics Association**:** 10.
Knox, H. A., J. B. Ajo-Franklin, T. C. Johnson, J. P. Morris, M. C. Grubelich, L. A. Preston, J. M. Knox and D. K. King (2016). Imaging Fracture Networks Using Joint Seismic and Electrical Change Detection Techniques. 50th U.S. Rock Mechanics/Geomechanics Symposium. Houston, Texas, American Rock Mechanics Association**:** 12.
Laubach, S. E., J. N. Hooker and R. Marrett (2014). "A universal power-law scaling exponent for fracture apertures in sandstones." GSA Bulletin **126**(9-10): 1340-1362.
Lee, S. H. and A. Ghassemi (2011). Three-Dimensional Thermo-Poro-Mechanical Modeling of Well Stimulation And Induced Microseismicity. 45th U.S. Rock Mechanics / Geomechanics Symposium. San Francisco, California, American Rock Mechanics Association**:** 13.
Long, J. C. S., J. S. Remer, C. R. Wilson and P. A. Witherspoon (1982). "Porous media equivalents for networks of discontinuous fractures." Water Resources Research **18**(3): 645-658.
Lu, J. and A. Ghassemi (2017). Geomechanics-Based Stochastic Analysis of Microseismicity for Analysis of Fractured Reservoir Stimulation With Application to Newberry EGS. 51st U.S. Rock Mechanics/Geomechanics Symposium. San Francisco, California, USA, American Rock Mechanics Association**:** 10.
Lu, J. and A. Ghassemi (2019). "Estimating natural fracture orientations using geomechanics based stochastic analysis of microseismicity related to reservoir stimulation." Geothermics **79**: 129-139.
McGarr, A., S. M. Spottiswoode, N. C. Gay and W. D. Ortlepp (1979). "Observations relevant to seismic driving stress, stress drop, and efficiency." Journal of Geophysical Research: Solid Earth **84**(B5): 2251-2261.
McTigue, D. F. (1986). "Thermoelastic response of fluid-saturated porous rock." Journal of Geophysical Research: Solid Earth **91**(B9): 9533-9542.
Meng, C. and H. Wang (2018). "A finite element and finite difference mixed approach for modeling fault rupture and ground motion." Computers & Geosciences **113**: 54-69.
Morris, J. P., P. Fu, P. Dobson, J. Ajo-Franklin, T. J. Kneafsey, H. Knox, D. Blankenship, M. D. White, J. Burghardt, T. W. Doe and E. G. S. C. Team (2018). Experimental Design for Hydrofracturing and Fluid Flow at the DOE EGS Collab Testbed. 52nd U.S. Rock Mechanics/Geomechanics Symposium. Seattle, Washington, American Rock Mechanics Association**:** 11.
Murphy, H., H. Keppler and Z. Dash (1983). Does hydraulic-fracturing theory work in jointed rock masses, Los Alamos National Lab., NM (USA); Bundesanstalt fuer Geowissenschaften und ….
Oldenburg, C., P. DOBSON, Y. WU, P. COOK, T. KNEAFSEY, S. NAKAGAWA, C. ULRICH, D. SILER, Y. GUGLIELMI and J. AJO-FRANKLIN (2016). "Intermediate-Scale Hydraulic Fracturing in a Deep Mine-kISMET Project Summary 2016: kISMET Project Summary 2016."
Pruess, K. (1992). Brief guide to the MINC-method for modeling flow and transport in fractured media, Earth Sciences Division, Lawrence Berkeley National Laboratory. Berkeley CA USA.
Rahman, M. K., M. M. Hossain and S. S. Rahman (2002). "A shear-dilation-based model for evaluation of hydraulically stimulated naturally fractured reservoirs." International Journal for Numerical and Analytical Methods in Geomechanics **26**(5): 469-497.
Rawal, C. and A. Ghassemi (2014). "A reactive thermo-poroelastic analysis of water injection into an enhanced geothermal reservoir." Geothermics **50**: 10-23.

Roggenthen, W. M. and T. W. Doe (2018). Natural Fractures and Their Relationship to the EGS Collab Project in the Underground of the Sanford Underground Research Facility (SURF). 52nd U.S. Rock Mechanics/Geomechanics Symposium. Seattle, Washington, American Rock Mechanics Association**:** 11.
Scotti, O. and F. H. Cornet (1994). "In Situ Evidence for fluid-induced aseismic slip events along fault zones." International Journal of Rock Mechanics and Mining Sciences & Geomechanics Abstracts **31**(4): 347-358.
Senatorski, P. (2019). "Effect of Slip-Weakening Distance on Seismic–Aseismic Slip Patterns." Pure and Applied Geophysics.
Shapiro, S. A., E. Huenges and G. Borm (1997). "Estimating the crust permeability from fluid-injection-induced seismic emission at the KTB site." Geophysical Journal International **131**(2): F15-F18.
Tezuka, K., T. Tamagawa and K. Watanabe (2005). Numerical simulation of hydraulic shearing in fractured reservoir.
Tezuka, K. and K. Watanabe (2000). Fracture Network Modeling of Hijiori Hot Dryrock Reservoir by Deterministic and Stochastic Crack Network Simulator(d/sc).
Ucar, E., I. Berre and E. Keilegavlen (2018). "Three-Dimensional Numerical Modeling of Shear Stimulation of Fractured Reservoirs." Journal of Geophysical Research: Solid Earth **123**(5): 3891-3908.
Ulrich, C., P. F. Dobson, T. J. Kneafsey, W. M. Roggenthen, N. Uzunlar, T. W. Doe, G. Neupane, R. Podgorney, P. Schwering, L. Frash and A. Singh (2018). the Distribution, Orientation, and Characteristics of Natural Fractures for Experiment 1 of the EGS Collab Project, Sanford Underground Research Facility. 52nd U.S. Rock Mechanics/Geomechanics Symposium. Seattle, Washington, American Rock Mechanics Association**:** 8.
Wang, X. (2014). Three-Dimensional FEM Modeling of Geothermal Reservoir Stimulation Using Stochastic Fracture Networks and Continuum Damage Mechanics. Ph.D. Dissertation, The University of Oklahoma
Wang, X. and A. Ghassemi (2012). A 3D Thermal-Poroelastic Model For Naturally Fractured Geothermal Reservoir Stimulation. 46th U.S. Rock Mechanics/Geomechanics Symposium. Chicago, Illinois, American Rock Mechanics Association**:** 10.
Wang, X. and A. Ghassemi (2012). A 3D thermal-poroelastic model for naturally fractured geothermal reservoir stimulation.
Willis-Richards, J., K. Watanabe and H. Takahashi (1996). "Progress toward a stochastic rock mechanics model of engineered geothermal systems." Journal of Geophysical Research: Solid Earth **101**(B8): 17481-17496.
Ye, Z. and A. Ghassemi (2018). "Injection-Induced Shear Slip and Permeability Enhancement in Granite Fractures." Journal of Geophysical Research: Solid Earth **123**(10): 9009-9032.
Ye, Z. and A. Ghassemi (2019). Failure Behavior of the Poorman Schist and Its Fractures from EGS Collab Stimulation Site. 44rd workshop on geothermal reservoir engineering, Stanford, California, USA.
Zhou, X. and A. Ghassemi (2009). "Finite element analysis of coupled chemo-poro-thermo-mechanical effects around a wellbore in swelling shale." International Journal of Rock Mechanics and Mining Sciences **46**(4): 769-778.

Rahman, M. K., M. M. Hossain and S. S. Rahman (2002). "A shear-dilation-based model for evaluation of hydraulically stimulated naturally fractured reservoirs." International Journal for Numerical and Analytical Methods in Geomechanics **26**(5): 469-497.Scholz, C. H. (2002). The mechanics of earthquakes and faulting, Cambridge university press.
Ye, Z. and A. Ghassemi (2018). Experimental Study on Injection-induced Fracture Propagation and Coalescence for EGS Stimulation.